eNeuro

Research Article: New Research | Integrative Systems

Differential stability of miR-9-5p and miR-9-3p in the brain is determined by their unique *cis*- and *trans*-acting elements

https://doi.org/10.1523/ENEURO.0094-20.2020

Cite as: eNeuro 2020; 10.1523/ENEURO.0094-20.2020

Received: 11 March 2020
Revised: 21 April 2020
Accepted: 25 April 2020

Differential stability of miR-9-5p and miR-9-3p in the brain is determined by their unique *cis*- and *trans*-acting elements.

Kim CK, Asimes A, Zhang M, Son B, Kirk JA, Pak TR

Loyola University Chicago, Stritch School of Medicine, Department of Cell and Molecular Physiology

Abbreviated Title: miR-9 degradation profiles in the brain

Author Contributions: CK designed and performed research, analyzed data, and wrote the paper; AA designed and performed research and contributed reagents; MZ performed research and edited paper; BS performed research and edited paper; JK designed research and edited paper; TP designed research, analyzed data, and wrote the paper.

Correspondence should be addressed to: tpak@luc.edu

Number of Figures: 8
Number of Tables: 3
Number of Multimedia: 0
Number of words in abstract: 248
Number of words in significance statement: 78
Number of words in Introduction: 717
Number of words in Discussion: 2182

The authors report no conflicts of interest

Support for this work was provided by NIA AG033605

Abstract

microRNAs (miR) are fundamental regulators of protein coding genes. In the central nervous system, miR-9 is highly enriched and critical for neuronal development and function. Mature miRs are derived from a duplex precursor, and the -5p strand ("guide") is preferentially incorporated into an RNA-induced silencing complex to exert its regulatory functions, while the complementary -3p strand ("passenger") is thought to be rapidly degraded. By contrast, both strands of the miR-9 duplex have unique functions critical for neuronal physiology, yet their respective degradation rates and mechanisms governing degradation are not well understood. Therefore, we determined the degradation kinetics of miR-9-5p and miR-9-3p and investigated the *cis* and *trans* elements that affected their stability in the brain. Using a combination of homogeneous neuronal/astrocyte cell models and heterogeneous brain tissue lysate, we demonstrate the novel finding that miR-9-3p was more stable than the miR-9-5p guide strand in all models tested. Moreover, the degradation kinetics of both miR-9-5p and miR-9-3p were brain-region specific, suggesting that each brain region was differentially enriched for specific degradation factors. We also determined that the 3' nucleotides harbor important *cis* elements required to not only maintain stability, but also to recruit potential protein degradation factors. We used mass spectrometry to assess the miR-9 interacting proteins and found that the -5p and -3p strands were associated with functionally distinct proteins. Overall, these studies revealed unique miR-9-5p and miR-9-3p degradation kinetics in the brain and propose critical nucleotide sequences and protein partners that could contribute to this differential stability.

Significance Statement

miR-9-5p and miR-9-3p are two single-stranded microRNAs (miR) derived from the same RNA duplex that are critical for normal neuronal function. Here, we report the differential degradation kinetics of these neuronally enriched miRs, as well as identify unique regulatory *cis* and *trans*

elements that could contribute to the distinct miR-9-5p and miR-9-3p stability in neurons. These findings contribute to the current understanding of how neuronal miRs are degraded and could have functional implications for their respective mRNA targets.

Introduction

Posttranscriptional regulation of protein-coding genes (mRNA) is a critical mechanism for maintaining cellular homeostasis. Cells must orchestrate a delicate balance between the synthesis of new molecules and the degradation and/or export of older ones. microRNAs (miRs) are a major contributor to this process, as it is estimated that they regulate over 60% of all protein-coding genes in eukaryotic cells (Friedman *et al*., 2009). The major steps for the biogenesis of miRs have largely been determined; however, the mechanisms of miR degradation are still the focus of ongoing research. Earlier reports suggested that miRs are globally more stable compared to mRNA (Gantier *et al*., 2011; Rüegger and Großhans, 2012; Zhang *et al*., 2012;), and this stability is thought to be imparted by miR association with RNA binding proteins, such as Argonaute 2 (AGO2). When bound to AGO2, structural analyses dictate that the 5' and 3' ends of the mature miR are embedded within the protein, thereby shielding it from potential exoribonucleases (Wang *et al*, 2008). Recently, mechanisms of TDMD (target-directed miR degradation) have been discovered whereby a highly complementary, endogenous RNA target is capable of dislodging the 3' end of the miR from the AGO2 PAZ domain, allowing it to be more accessible to *trans* factors responsible for RNA tailing, trimming, and ultimately degradation (Park *et al*., 2017; Bitetti *et al*., 2018; Ghini *et al*., 2018; Kato, 2018; Wightman *et al*., 2018). The reported mechanisms of TDMD suggest that *cis* sequence motifs of the miRs, as well as the recruitment of *trans* acting proteins to the site of degradation, are crucial determinants of miR degradation kinetics; however, the specifics of these factors remain elusive.

To further add to the complexity of miR degradation, miRs exhibit varying half-lives between different tissues and cell types within an organism (Li *et al*., 2013). For example, miR stability in the central nervous system is a striking exception to the long half-lives generally observed in peripheral organs. Neuronal miRs are highly unstable and can be regulated by neuronal activity, suggesting that their silencing function is temporally controlled by external stimuli (Krol *et al*., 2010; Fu *et al*., 2016). Indeed, a variety of chemical and electrical stimuli has been shown to dramatically alter miR expression levels in cultured neurons (for review Sim *et al.,* 2014), adding another layer of regulation to the unstable nature of neuronal miRs. Notably, the half-life of one of the most abundant neuron-enriched miRs, miR-9-5p, was reported to be less than one hour in primary neocortical cells (Sethi *et al*., 2009). However, the degradation kinetics of its duplex counterpart, miR-9-3p, was not considered in this study. miR-9-5p is designated as the “guide” strand in most deuterostomes, and its annotation is derived from the mature miR sequence being embedded in the 5’ stem of the miR-9 precursor; conversely, miR-9-3p, or the “passenger” strand, is embedded in the 3’ stem. For most miRs, it is generally accepted that the guide strand of the duplex is preferentially loaded onto AGO2 and is the functionally relevant strand, while the passenger strand is quickly degraded. However, both miR-9-5p and miR-9-3p are neuron-enriched, and their individual functional contributions have been extensively described in regulating critical neuronal processes such as driving neuronal differentiation, initiating angiogenesis, and modulating synaptic plasticity (Yuva-Aydemir *et al*., 2011; Coolen *et al*., 2013; Sun *et al*., 2013; Giusti *et al*., 2014; Richner *et al*., 2015; Sim *et al*., 2016; Madelaine *et al*., 2017). The significance of their individual functions implies that both the -5p and -3p transcripts must be relatively stable and separately loaded onto AGO2; however, the degradation kinetics of these two miRs, especially miR-9-3p, are not well characterized in the literature. Therefore, the studies herein focused on discerning the relative degradation kinetics of miR-9-5p and miR-9-3p due to their neuronal enrichment and their significant roles in regulating neuronal physiology.

The objective of this study was to determine the relative degradation kinetics and the factors that govern miR-9-5p and miR-9-3p degradation specifically in the rat hypothalamus and ventral hippocampus: regions of the brain that regulate homeostasis in a variety of physiological processes. Moreover, previous studies showed that miR-9-5p and miR-9-3p expression increased with advanced age in these brain regions (Rao *et al*., 2013). Therefore, in this study, we investigated miR-9 degradation kinetics in aged rats (18-months) when expression levels were highest, underscoring the possibility that the kinetics of miR turnover would be functionally relevant. We hypothesized that the degradation kinetics of miR-9-5p in the aged hypothalamus would be distinct from that of miR-9-3p. Moreover, we predicted that any differences in miR degradation kinetics would be due to intrinsic differences in nucleotide composition (i.e. *cis* factors) or through differential recruitment of *trans* factors that contribute to degradation processes. These possibilities were tested *in vivo* using a rat model and *in vitro* using hypothalamic-derived neuronal cells lines. Collectively, our results indicate that miR-9-5p stability is distinct from that of miR-9-3p, and this difference can be explained, in part, by their unique *cis* and *trans* elements.

Materials and Methods

Animals. Female rats (Wistar, 5 months old; Fisher344, 18 months old, NIH aging colony) were obtained from Charles River Laboratories. Previous studies showed that miR-9-5p and miR-9-3p steady-state expression increased with age in the rat hypothalamus and ventral hippocampus (Rao *et al*., 2013). Therefore, in this study, we used old (18-month) Fisher344 rats. Rats were pair-housed on arrival and allowed to acclimate for 1 week prior to further experimentation. Rats were supplied with standard rat chow and tap water *ad libitum*, and animals were kept on a 12:12 light/dark cycle with ZT0 at 7:00 AM. All animal protocols were approved by Loyola University Chicago Animal Care and Use Committee (IACUC, permit

2009018). Experiments were conducted in accordance to the guidelines set forth by the IACUC, and all appropriate measures were taken to minimize pain and suffering.

Cell culture. IVB cells, a neuronal cell line derived from rat hypothalamus (provided by John Kaskow, University of Cincinnati), were grown to 70~80% confluency in Dulbecco's Minimum Essential Medium (DMEM) media containing glucose, L-glutamine, sodium pyruvate, and 10% fetal bovine serum (FBS). Cells were subsequently lysed using a 0.5% NP40 buffer with protease and phosphatase inhibitors (Thermo Fisher Scientific, #PI88669). Following cell lysis, protein concentration was determined using a BCA assay according to manufacturer instructions (Thermo Fisher Scientific, #23225).

Actinomycin treatment. IVB cells were treated with actinomycin D (Sigma Aldrich, A9415) at a final concentration of 10 µg/mL for 2 hours in order to inhibit transcription. Actinomycin D was diluted in dimethyl sulfoxide at a stock concentration of 1 mg/mL prior to addition to cell culture media. Cells were lysed at three different time points: T0, 15 min., and 60 min. These experiments were performed independently using 5 different cell passages.

RNA isolation and cDNA synthesis. Total RNA was isolated from IVB cells using the Zymogen DirectZol Kit. 1.0 µg of RNA was reversed transcribed using the Norgen miRNA cDNA Synthesis Kit (#54410) according to manufacturer instructions.

RT-qPCR. RT- qPCR for miR-9-5p and -3p was performed using forward primers specific to the mature sequence and a Universal Reverse Primer provided by the Norgen miRNA cDNA Synthesis Kit (#54410). All reactions were performed in triplicate. 18s rRNA was used as a loading control to normalize the data for $\Delta\Delta$Ct analysis. The following cycling conditions were

used: 1) 95 °C for 10 minutes, 2) 95 °C for 15 seconds, 3) 59 °C for 20 seconds, 4) 72 °C for 12 seconds, and melting curve analysis.

Primary astrocytes. Primary astrocytes were obtained from the cortex of 5 month old, female Wistar rats (N = 3). Cortical tissue was digested using 0.25% trypsin-EDTA, and neuronal cell growth was inhibited with the addition of DMEM: F12 media supplemented with 0.1 mg/mL primocin following the plating procedure. Primary astrocytes were grown to 70~80% confluency in the following astrocyte medium: Dulbecco's Minimum Essential Medium (DMEM) 50:50 F12 media containing glucose, L-glutamine, sodium pyruvate, and 10% fetal bovine serum (FBS).

In vivo tissue preparations. 18 month old female Fisher 344 rats were killed (N = 3), and whole brain was isolated and flash frozen in 2-methylbutane at -30°C. Flash frozen brains were sectioned at 200 µm on a freezing microtome, and regions of interest were microdissected using a 0.75 mm Palkovit's brain punch tool (Stoelting Co., Wood Dale, IL; [POA: preoptic area (-.26 to -1.4 mm relative to bregma), SON: supraoptic nucleus (-.8 to -3.14 mm relative to bregma), vHIPP: ventral hippocampus, (-4.16 to -5.8 mm relative to bregma)] utilizing *The Rat Brain in Stereotaxic Coordinates* (Academic Press, 1986) as a reference. Brain tissue lysate was prepared as described above. Selected samples from the SON brain tissue lysate were treated with 250 µg/mL proteinase K (ThermoFisher Scientific, #25-530-049) and incubated for 1 hour at 60°C before using in the miR degradation assay.

miR degradation assay. The miR degradation assay was adapted for tissue and whole cell lysates based on methods described by Chatterjee and colleagues (Chatterjee *et al*., 2009). Briefly, oligonucleotide constructs were synthesized with the exact nucleotide sequence of the mature transcript for miR-9-5p and miR-9-3p, [UCUUUGGUUAUCUAGCUGUAUGA] [AUAAAGCUAGAUAACCGAAAGU], respectively (Integrated DNA Technologies, Coralville, IA).

These single stranded oligonucleotide sequences were then radiolabeled on the 5' end using [γ32P] ATP (3000 Ci/mmol) (Perkin Elmer, Waltham, MA). 10 fmols of the newly radiolabeled sequence was then incubated with 20 µg of protein from either the IVB cell lysate or brain tissue lysate prepared as described above. Incubation of the radiolabeled miR with the lysate was terminated at 5 different time points by boiling at 95°C for 2 min. following the addition of 2X RNA Loading Dye (New England Biolabs, #B0363S). The resulting mixture was then resolved on an 8% urea gel by electrophoresis. Finally, the gel was visualized by phosphoimaging (GE Healthcare, Typhoon) to detect levels of the radiolabeled miR at the various time points. Gel bands were quantified using densitometry analyses with ImageJ (RRID:SCR_003070) software and averaged densitometry values from multiples replicates were plotted on a scatterplot using OriginLab software. Degradation kinetics were determined using a best-fit exponential decay function.

AGO2 immunoprecipitation. 20 µg of IVB protein lysate was premixed with anti-AGO2, anti-AGO4, β-actin, or IgG antibody (Wako #22023, RRID:AB_1106837; Cell Signaling #6913, RRID:AB_10828811; Cell Signaling #4970, RRID:AB_2223172; Millipore #12-370, RRID:AB_145841) overnight at 4°C. The preformed antibody-antigen complex was then added to 50 µl of PureProteome Protein A/G Magentic Beads (Millipore, #LSKMAGAG02) and incubated for 30 min. at room temperature. Next, 10 fmols of radiolabeled miR were added to this mixture and incubated at 37°C for 15 min. The Pureproteome magnetic stand was used to capture the beads, and three washes were performed with PBS containing 0.1% Tween 20 detergent. After the last wash, the bound protein complexes were eluted with the addition of 0.5% NP40 buffer and 2X RNA Loading Dye (New England Biolabs, #B0363S) followed by boiling at 95°C for 2 min.

RNA Immunoprecipitation. 500 µg of vHipp lysate, 1 µg of biotinylated RNA (Integrated DNA Technologies, Coralville, IA), 10X protease inhibitor (ThermoFisher Scientific, #PI88669), 40U/µL RNase inhibitor (ThermoFisher Scientific, #10-777-019), and 2X TENT buffer (20mM Tris-HCl, 2mM EDTA, 500mM NaCl, 1% Triton X-100) were mixed and incubated at room temperature for 30 min. RNA-protein interactions were fixed using formaldehyde at a 1% final concentration for 10 min. 50 µL of Dynabeads MyOne Streptavidin C1 (ThermoFisher Scientific, #65002) was then added to the above mixture and incubated for another 30 min. at room temperature. This mixture was placed on a PureProteome magnetic stand, (Millipore Sigma, #LSKMAGS08) and the beads were washed 3 times with 1X TENT buffer before final elution with 40 µl of 1X laemmli buffer (Bio-Rad, #161-0747) at 95°C for 5 min. The eluted proteins were then run on a 10% SDS PAGE gel at 120 mV for 60 min. and proteins were visualized by Coomassie staining (R250).

In gel digestion. Protein bands were cut into 1 mm^3 pieces and washed with 100 mM ammonium bicarbonate shaking at 600 RPM for 15 min. at 37°C. The gel pieces were then washed with a 50:50 100 mM ammonium bicarbonate and acetonitrile solution at 600 RPM for 15 min. at 37°C. The final wash was performed with 100% acetonitrile at the same conditions as the previous washes. The gel pieces were reduced with 250 mM DTT (Sigma-Aldrich, #D9779-5G) at 550 RPM for 60 min. at 56°C and subsequently alkylated with 50 mM iodoacetamide (Sigma-Aldrich, #A3221-10VL) in the dark for 45 min. at room temperature. Finally, 2 µg of MS grade Trypsin (ThermoFisher Scientific, #PI90057) was added to the gel pieces to digest the protein overnight at 37°C while shaking at 600 RPM.

Mass spectrometry. The analysis was carried out on a Dionex Ultimate 3000 RSLCnano coupled to a LTQ Orbitrap XL (ThermoFisher Scientific). 10 µL of each sample was injected onto the column. Mobile phase A was 100% H_2O, 0.1% formic acid, and mobile phase B was

80% ACN, 0.08% formic acid. The flow rate was set at 300 nL/min. The column oven was set at 40°C. A gradient of 5 – 45% mobile phase B was run over 105 min. followed by a wash cycle and equilibration of the column. Total run time on the HPLC was 138 min. An EASY-spray column (2 µm particle size, 25 cm x 75 µm ID, PepMap C18) was used to separate the peptides, and an EASY-Spray ionization source was used for ionization. Data dependent acquisition was carried out with the mass spectrometer. The first scan was recorded with the Orbitrap followed by 10 subsequent ion trap scans (FT-IT detection) on the top 10 most abundant ions. Collision Induced Dissociation (CID) was used as the activation source with normalized collision energy at 35. Charge state rejection was enabled for +1 charged ions, and dynamic exclusion was enabled for a list size of 500 over 30 seconds. The data was analyzed using PEAKS 8.5 software.

Statistics. All statistical analysis was performed using OriginLab software. A two-sample T-test was performed to compare the mean half-lives of miR-9-5p and miR-9-3p in cell lines. The actinomycin D experiments were analyzed using a two-way ANOVA with time and miR construct as the two factors. The brain region specific degradation of miR-9-5p and -3p was also analyzed using a two-way ANOVA with brain region and miR construct as the two factors. A one-way ANOVA was performed to compare the mean densitometry values of the various miR-9-5p constructs at the T1 time point. A Tukey's post hoc test was subsequently performed to determine statistically significant differences between group means. All data points are displayed as mean ± SEM, and statistical significance was noted when $P < 0.05$.

Results

The "passenger strand" miR-9-3p was more stable than the "guide strand" miR-9-5p in a hypothalamic cell line

We used a basic biochemical approach to determine if the unique nucleotide sequence of miR-9-5p and miR-9-3p affected their degradation kinetics when exposed to identical cellular lysate components. Importantly, to our knowledge, this assay has only been done previously in cell-free conditions making this the first study to observe the degradation products of these miRs following exposure to native cell and whole tissue constituents. First, ^{32}P-labeled oligonucleotides identical to each miR were incubated in cell lysate purified from hypothalamic-derived neuronal cells (IVB). The cells were subjected to a mild lysis buffer that was not likely to disrupt the nuclear envelope, as we hypothesized that most miR degradation factors would reside in the cytoplasm. Each construct was first visualized at the correct size compared to a nucleic acid ladder size marker (Fig. 1A). Next, radiolabeled miR-9-5p and miR-9-3p were incubated in IVB lysate for 5 different time points (T0, 15, 60, 120, 240 min.). Our results showed that miR-9-3p, canonically considered the passenger strand, was more stable than miR-9-5p (Fig. 1B, C). Roughly ~50% of the full length miR-9-5p signal was reduced at the 15 minute time point, and by the 1 hour time point, the full length signal was completely abolished. Comparatively, the signal corresponding to full length miR-9-3p was significantly higher than miR-9-5p at the 1 hour time point, indicating slower degradation kinetics ($p = 0.048$, Fig. 1B, D). A comparison of the mean half-lives derived from the best-fit exponential decay functions indicated that miR-9-3p was approximately twice as stable as miR-9-5p, exhibiting half-lives of 31.85 and 13.09 min., respectively (Fig. 1C, E). Importantly, a small fraction of both radiolabeled constructs (miR-9-5p and miR-9-3p) were shown to bind AGO2, but not AGO4 or β-actin, demonstrating that the radiolabeled miRs bind specifically to relevant RNA binding proteins in this assay (Fig. 1-1).

We also observed size differences in the miR-9-5p and miR-9-3p degradation products (i.e. smaller size bands on the gel), suggesting that the miRs were cleaved at different locations. Specifically, miR-9-5p had 4 discrete bands corresponding to the degradation products, whereas miR-9-3p only had 2 discrete bands (Fig. 1B). Next, we used a second method to

verify that miR-9-3p was more stable by measuring the degradation rates of endogenously expressed mature miR-9-5p and miR-9-3p following transcriptional inhibition with actinomycin D. Consistent with the miR degradation assays, these experiments also showed that miR-9-3p was more stable than its miR-9-5p counterpart (Fig. 2). Two-way ANOVA analysis revealed that there was a significant main effect of miR construct (Table 1.). Subsequent post hoc analyses using Tukey's HSD revealed that at the one hour time point, miR-9-3p levels were significantly higher ($p = 0.049$) compared to miR-9-5p, indicating a more stable profile (Fig. 2). Notably, this assay used intact live cells and confirmed that the relative stability of miR-9-3p compared to miR-9-5p was similar to the purely biochemical approach of the miR degradation assay described above.

miR-9-3p was more stable than miR-9-5p in a brain region dependent manner

Next, the degradation kinetics of miR-9-5p and miR-9-3p were investigated using brain tissue lysate from 3 different rat brain regions: the preoptic area (POA), the ventral hippocampus (vHIPP), and the supraoptic nucleus (SON). These regions were selected due to previous reports demonstrating endogenous miR-9-5p and miR-9-3p expression in these regions (Rao *et al*., 2013; 2015). Unexpectedly, the time course for both miR-9-5p and miR-9-3p degradation in each of these brain regions was consistently faster than what was observed in the hypothalamic IVB neuronal cell lines, even though total protein concentrations were identical in the different lysates (Fig. 3A, B). The signal corresponding to the full length miR-9-5p disappeared almost immediately upon exposure to brain tissue lysate; therefore, T0 had to be redefined using lysis buffer alone to determine the correct starting concentration, and the time scales were adjusted accordingly to T0, 1, 15, 60, and 120 min. (Fig. 3A). Our results also showed brain region specific differences in miR-9-5p degradation. For instance, the signal corresponding to full length miR-9-5p was present at the 1 minute time point in POA lysate, but absent in vHipp and SON lysate (Fig. 3A). A two factor ANOVA analysis of miR half-lives

showed that there was a statistically significant main effect of brain region (factor 1) and a significant main effect of miR construct (factor 2). There was also a statistically significant interaction between brain region and miR construct, demonstrating that the degradation rate of each miR was dependent on brain region (Table 1). Consistent with the data observed in the IVB cell line, the half-life of miR-9-3p was significantly longer in all three brain regions compared to miR-9-5p (Fig. 3C). Full length miR-9-3p persisted to the 15 minute time point in every brain region. However, differential degradation kinetics for miR-9-3p were still observed dependent on brain region, as miR-9-3p exhibited a longer half-life in the SON and POA compared to the vHipp (Fig. 3C). These data suggest that miR degradation might occur rapidly in the intact rat brain, but there are also distinct region-dependent kinetics.

Rapid miR-9-5p degradation in vivo was dependent on protein concentration of the lysate

The rapid degradation of miR-9-5p and miR-9-3p that was observed in the brain tissue lysate suggested that there could be enriched levels of specific miR degradation factors compared to the cell lysate. Therefore, to determine whether rapid degradation of miR-9-5p adhered to first order degradation kinetics, radiolabeled miR-9-5p was incubated in various dilutions of SON lysate (1:10, 1:100, 1:1000) for the miR degradation assay. The SON was utilized for these experiments, because this was the region where miR-9-5p exhibited the fastest degradation (Fig. 3B). The results showed a steady increase in miR-9-5p stabilization upon increased lysate dilution, culminating in the complete elimination of any degradation products after 4 hours of incubation at a dilution of 1:1000 (Fig. 4A, B). We also hypothesized that the unknown miR degradation factors present in the brain tissue lysate were proteins, and not nucleic acids, steroids, or other chemical compounds. To test this hypothesis, we performed the same assays using lysis buffer alone (i.e. no lysate present) and compared that to proteinase-K treated SON lysate (Fig. 4A). Our results demonstrated that miR-9-5p was stable across all time points in both of these treatment groups, suggesting that an unknown protein of fairly high

abundance was present in the brain tissue lysate and likely contributed to rapid miR-9-5p degradation.

Degradation of miR-9-5p was slower in primary astrocytes compared to whole brain tissue lysate.

Brain tissue lysate is a heterogeneous cell population consisting primarily of neurons and various types of glial cells. We predicted that the glial contribution might account for the enhanced rate of degradation observed in brain tissue lysate compared to the slower rate observed in the homogenous neuronal cell lysate (i.e. IVB cells). Therefore, we used primary astrocytes isolated from the rat brain to determine the contribution of glial cells to miR-9-5p degradation. Contrary to our prediction, miR-9-5p degradation kinetics were relatively stable when incubated with astrocyte only lysate. Specifically, the full length miR-9-5p signal could be detected at the 15 minute time point (Fig. 5A, B), suggesting that there are inherent differences in miR degradation kinetics between immortalized neuronal cell lines and neurons from the rat brain. Further, the average half-life was 17.84 min. closely resembling the profile we observed with the neuronal cell lysate (IVB cells) (Fig. 5C).

Nucleotide sequences at both the 5' and 3' end contribute to miR-9 stability

One possible explanation for the observed degradation differences in miR-9-5p and miR-9-3p was the distinct nucleotide sequences (i.e. *cis* factors) of each miR, especially considering that differences in degradation rates and cleavage products occurred despite both miRs being exposed to identical lysate conditions. Moreover, the presence of multiple degradation products for miR-9-5p and miR-9-3p suggested that at least some of the degradation occurred in a 3' to 5' direction, due to the radiolabeled phosphate being located at the 5' position and subsequent visibility of a smaller radiolabeled products on the gel. Therefore, to test the importance of the 3' end nucleotide sequence in determining stability, the last 3 nucleotides of miR-9-5p and miR-9-

3p were exchanged to create two new chimeras: 5p* and 3p*. The 5p* chimera had a UGA to AGU substitution at the 3' end, while the 3p* had an AGU to UGA substitution (Fig. 6A). Our results demonstrated that swapping just 3 nucleotides at the 3'end of miR-9-5p with miR-9-3p (i.e. the *5p construct) was sufficient to significantly increase the stability of miR-9-5p at 1.0 min. when incubated with lysate taken from the SON ($p = 0.004$; Fig. 6B, D). Conversely, this swap had the opposite effect on miR-9-3p (i.e. the 3p* construct) with it showing significantly faster degradation at 15 min. compared to its native sequence ($p = 0.045$; Fig. 6B, E). Therefore, swapping the 3' end nucleotides caused miR-9-5p to degrade at a more similar rate as miR-9-3p and vice-versa, suggesting that this sequence motif directly contributed to miR degradation kinetics (Fig. 6D, E).

It was evident that some amount of degradation also occurred from the 5' end, based on a small decrease in the relative intensity of the gel bands from the initial incubation time point to the final time point. Therefore, we altered miR-9-5p to match that of a documented endogenous isomiR to determine the contribution of 5' nucleotides to the degradation profile. This isomiR is endogenously generated from alternative Drosha cleavage and results in one less uracil at the 5' terminal end of the miR (Bofill-De Ros *et al*., 2019). Interestingly, the miR-9-5p isomiR tended to be more stable than the miR-9-5p annotated as the wildtype ($p = .065$; Fig. 6B, D). Together, these data provide evidence that *cis* elements at both the 5' and 3' ends of the miR are critical for determining its degradation kinetics.

miR-9-5p and miR-9-3p were associated with distinct proteins in the ventral hippocampus

The contribution of unique *cis* elements to miR degradation rates suggested that these specific nucleotide sequences might recruit different *trans* factors, which then resulted in distinct degradation products for miR-9-5p and miR-9-3p. Our data also demonstrated that miR degradation was dependent on unknown proteins present in the brain tissue lysate (Fig. 4B). Therefore, we analyzed the proteins associated with each miR using a discovery-based mass

spectrometry approach to determine if these miRs were associated with distinct proteins that might be involved in RNA degradation processes. The ventral hippocampus was used for the proteomic studies as it represented a relatively large region of the brain compared to smaller specific hypothalamic nuclei, allowing for a sufficient starting concentration of protein. Biotinylated miR-9-5p and miR-9-3p (Fig. 7A) were incubated with vHipp lysate, and bound proteins were eluted and run on a 10% SDS PAGE gel. We focused on identifying proteins from prominent bands present at the 45 ~ 55 kDa range that was evident upon electrophoresis of proteins following streptavidin-bead purification (Fig. 7B). These bands were subsequently digested into smaller peptide fragments and analyzed by mass spectrometry.

We also analyzed the proteins that were associated with the approximated degradation products of miR-9-5p and miR-9-3p in the vHipp by creating biotinylated sequences that were shorter in length from the 3' direction (16 and 12 nucleotides each) (Fig. 7A). These shortened constructs were selected due to the relative stability of the degradation products compared to the full-length transcript. Interestingly, the proteins associated with these shortened constructs were also enriched at the 45 ~ 55 kDa molecular weight range (Fig. 7B). Mass spectrometry analysis revealed full-length miR-9-5p had 9 unique associated proteins compared to 7 unique proteins for miR-9-3p (Fig. 7C, Table 2). The shortened miRs also had distinct proteins associated with them, not only between the -5p and -3p transcripts, but also compared to their own respective full-length transcripts (Fig. 7 C, D; Table 2). We used Panther gene ontology software to analyze the identified proteins according to their function, and the most represented functional class for full-length miR-9-5p was related to cellular metabolism (~33%, Table 3). In contrast, the most represented functional class of proteins captured by full-length miR-9-3p was related to cytoskeletal organization and transport (~57%, Table 3). Moreover, approximately 44% of the 9 unique proteins identified for miR-9-5p were previously reported to have RNA binding capabilities.

Overall, the total number of identified proteins was reduced for each miR as its

sequence was progressively shortened. However, the representation of metabolism-related proteins remained high in the proteins associated with both the full-length and the 16 nT miR-9-5p fragment (Fig. 7D; Table 3). Similarly, both the full-length miR-9-3p and its 16 nT fragment was associated with CAVIN1 (caveolae associated protein 1), a protein implicated in ribosomal RNA synthesis, but this association was lost at the 12 nT length (Fig. 7D). The proteins associated with the 12 nT fragment (miR-9-3p) also did not have a dominant functional class, but PLRG1 (pleiotropic regulator 1), a spliceosomal component, was identified as a potential binding partner. The proteins associated with the 12 nT (miR-9-5p) fragment were again most represented in protein classifications pertaining to metabolism and cytoskeletal organization (~60%), suggesting that miR-9-5p retains proximity to proteins in the same functional milieu despite its degradation (Fig. 7D; Table 3). Overall, these data identified potential interactions between the miR-9-5p and miR-9-3p degradome and other RNA processes such as splicing, mRNA processing, and ribosomal RNA synthesis in the rat ventral hippocampus.

Discussion

The determinants of miR degradation kinetics in the context of the central nervous system are poorly understood. In the present study, we describe the novel finding that miR-9-3p was more stable than its duplex counterpart, miR-9-5p, when exposed to identical neuronal cell lysates. Our current view of miRs dictates that the mature strand designated as the “guide”, often derived from the 5’ stem of the pre-miR, is more stable than the strand designated as the “passenger”, making these data a novel and likely biologically relevant finding. Moreover, our data demonstrated that the relative stability of each strand was dependent on their unique *cis* factor sequence motifs residing at the 3’ end, perhaps through recruitment of distinct degradation factors that are unique to each miR. Indeed, we identified potential *trans* acting factors that were differentially associated with not only full length miR-9-5p and miR-9-3p, but also to their approximated degradation products. We also showed that the relative abundance of

the protein factors contributing to the differential degradation rates of miR-9-5p and miR-9-3p was likely different depending on brain region. Taken together, these data contribute to the current understanding of miR degradation kinetics, specifically in the biologically relevant context of the female rat brain.

Our data are consistent with previous studies suggesting that miRs in the brain are degraded rapidly, underscoring the importance of understanding how these relatively unstable miRs are able to exert functional effects downstream. miR-9-5p and miR-9-3p have repeatedly been shown to be neuron-enriched, and previous studies have demonstrated a negative correlation between miR stability and overall expression (Li *et al*., 2013). Neuronal miR-9-5p and miR-9-3p seem to follow this pattern: they are both highly expressed and rapidly degraded (Sethi *et al*., 2009; Amar *et al*., 2012), supporting a model whereby there is constitutive production and turnover of these particular transcripts. A potential benefit of such steady state kinetics is readily apparent in the context of neuronal systems in which the cell could quickly respond to dynamic changes in extracellular input, such as changes to synaptic firing frequency. Indeed, an example of activity-induced changes to miR stability was observed in retinal neurons responding to changes to light/dark stimuli (Krol *et al*., 2010). The relative stability of miR-9-3p that was observed from our data, (Fig. 1D, Fig. 3C) suggests that the -3p strand could have a more prominent role in regulating neuronal function compared to its -5p counterpart, making the 'guide' and 'passenger' designation somewhat arbitrary in neuronal physiology. This assertion is supported in a previous report demonstrating that miR-9-3p, but not -5p, was involved in the regulation of hippocampal memory and synaptic plasticity (Sim *et al.,* 2016).

Another novel finding of this study was the identification of distinct protein binding partners for miR-9-5p and miR-9-3p (Fig. 7C), and to our knowledge this study is the first to identify proteins associated with these mature miRs and their shorter degradation products. Eukaryotic translation initiator 5 (EIF5) was one identified protein that was associated with the full length miR-9-5p, but not miR-9-3p, in the vHIPP (Fig. 7C). EIF5 has been shown to interact

476 with EIF1A via its C-terminal domain (Luna *et al.,* 2013), and EIF1A is a recently discovered
477 component of the RNA-induced silencing complex (RISC) (Yi *et al.,* 2015). These data raise the
478 possibility that an EIF1A:EIF5 complex could be associated directly, or indirectly, with miRs that
479 are loaded onto RISC. Another interesting protein that was identified in the vHipp was tRNA
480 ligase, as it was shown to only associate with the approximated miR-9-5p degradation product
481 (16nt) (Fig. 7D). Recently, tRNA fragments have been shown to be loaded onto AGO and even
482 exert gene regulatory functions (Kuscu *et al*., 2018), suggesting potential crosstalk between the
483 molecular pathways of tRNA and miR degradation products.

484 The importance of the proteins that we found associated with the shorter miR fragments
485 (i.e. the approximated degradation products) is unclear. The proteins appeared to be specific to
486 each size product (16 vs. 12 nT), and the total number of associated proteins were reduced as
487 the nucleotide sequence was progressively shortened (Fig. 7C-E). Direct and specific protein
488 binding would suggest that these miRs could be functional and potentially bind to the same
489 targets as the full-length parent, given that the entire 8 nT seed sequence remained intact.
490 There is no evidence that these short fragments can bind to AGO proteins making it unlikely that
491 any functional effect would be similar to the full-length miR; however, these highly stable short
492 fragments could block the ability of a full-length miR to bind to its mRNA target through
493 competition at the seed sequence. The shorter degradation products were much more stable
494 than the full length miRs, and one possibility is that the associated proteins are important for
495 maintaining the stable expression of these fragments. However, it is important to consider that
496 due to the crosslinking reaction required for immunoprecipitation, the identified proteins
497 represent only those that were in close proximity with the biotinylated miR of interest and do not
498 necessarily reflect direct binding.

499 The myriad of molecular factors contributing to the rapid degradation of miRs in neurons
500 have still not been fully elucidated. One possibility is that neuronal miRs are partially regulated
501 by the process of target-directed miR degradation (TDMD) (Park *et al*., 2017; Bitetti *et al*., 2018;

Ghini *et al*., 2018; Kato, 2018; Wightman *et al*., 2018). Indeed, it has been reported that TDMD occurs to a higher degree in primary neurons compared to fibroblasts (de la Mata *et al*., 2015), but it remains to be seen if RNA-mediated degradation of miRs can fully explain rapid turnover kinetics. Our data showed that elimination of the cellular proteins, but not RNAs, through pre-digestion with proteinase K was sufficient to stabilize the normally rapidly degraded miRs for up to four hours (Fig. 4A, B), raising the possibility that the primary contribution of other cellular RNAs is to recruit the proteins required for miR degradation.

Our data using brain tissue lysate would suggest that miR-9-5p and miR-9-3p are degraded on a seconds-to-minutes time scale, respectively. However, Winter and Diederichs showed that the expression of AGO proteins was critical in determining global miR stability (2011), and we estimated that less than 10% of our input miR were efficiently loaded onto AGO2 (Fig. 1-1). Importantly, the loading efficiency was similar for both miR-9-5p and miR-9-3p, suggesting that the relative stability of miR-9-3p was the result of differential degradation. However, it is difficult to estimate how much endogenously expressed miR-9 is loaded onto AGO2 at any given time, and these numbers have not been reported to our knowledge. Nevertheless, we expect that the degradation kinetics reported in this study are likely reflective of the mature miR after it has unloaded from the RNA-induced Silencing Complex (RISC), thus leaving the single stranded transcript exposed to the cytoplasmic milieu. Notably, Baccarini *et al.* reported that a single miR can be recycled to have multiple mRNA targets, leaving the intriguing possibility that mature miRs can be reloaded onto AGO proteins after the completion of their initial RNAi function (2011). Nevertheless, our data provide valuable information about the *cis* features of miR-9-5p and miR-9-3p that contribute to differential stability. This modified assay (Chatterjee *et al*., 2009) used physiologically relevant levels (10 fmols) of miRs, in the context of cellular factors that are endogenously present in neurons, thereby allowing us to assess inherent sequence and/or structural features of each miR that contributes to stability. Our data clearly demonstrate that in brain tissue, each miR exhibited different rates of

degradation and resulted in different cleavage products, which were also brain-region specific, despite being subjected to identical experimental conditions. While it is still unclear which enzyme was responsible for the degradation that we observed, it is evident that miR-9-5p degradation was directly correlated with total protein concentration in the lysate based on our dilution experiments and digestion of proteins with proteinase K (Fig. 4A, B). Furthermore, the rapid degradation that was observed using tissue lysate suggests that a unique protein is present in brain tissue lysate compared to homogenous neuronal cell lines, as protein concentration was held constant for both experiments. It is also possible that extracellular RNases could have contributed to the acceleration of the decay kinetics. However, our experiments showing that there were brain-region specific differences suggest that the majority of degradation was most likely due to region specific expression of intracellular proteins that were critical for differential stabilization and not due to extracellular RNases. In addition, miR-9-5p was relatively stable in primary astrocytes (Fig. 5B, C), suggesting that the enzyme responsible for rapid degradation might be unique to neurons or have relatively lower expression in astrocytes.

Previous studies have used transcriptional inhibition, such as with actinomycin D, followed by qPCR to profile degradation kinetics of mature miRs (Sethi *et al*., 2009). Our own results from transcriptional inhibition studies indicate that miR-9-3p was again more stable than miR-9-5p under those conditions; in fact, miR-9-3p levels remained stable throughout all the time points that were measured (Fig. 2). While these studies are beneficial in that turnover kinetics can be measured in intact cells, transcriptional inhibition has been repeatedly shown to negatively affect cellular growth and survival. Therefore, it remains unclear how the turnover kinetics in these altered physiological contexts reflect those of native cells. Recent approaches utilizing metabolic labeling can circumvent many of the obstacles posed by transcriptional inhibition (Marzi *et al*., 2016). In those experiments, 4-thiouridine, a nucleoside analogue, is added to the cellular growth medium and incorporated by nascent RNAs that are actively

554 transcribed. This analogue is often modified by biotinylation so that it can be efficiently isolated
555 from the endogenous pool of RNA. The purified transcripts are then quantified by qPCR or other
556 sequencing methods to determine the steady state of the specific RNA of interest. However,
557 due to the intrinsic disparity in the uridine content of miR-9-5p and miR-9-3p, ~48% and ~18%
558 respectively, the purification efficiency of biotinylated 4-thiouridine in each of these miR
559 transcripts is also likely to be different, making it difficult to compare their rate of degradation. In
560 fact, Rädle and colleagues concluded that short RNA species with low uridine content are likely
561 to escape biotinylation-mediated precipitation even at high 4SU starting concentrations (2013).
562 Although metabolic labeling might best approximate the half-lives of miRs under normal
563 cellular conditions, it does not easily allow for biochemical manipulations that are necessary to
564 parse out both *cis* and *trans* factors of a specific RNA that could be important for determining its
565 degradation kinetics. For instance, our data indicated that simply altering 3 nucleotides at the 3'
566 end was sufficient to alter the degradation kinetics of both miR-9-5p and -3p to an intermediary
567 degradation rate (Fig. 6C), suggesting that the 3' end of mature miR-9 represents a critical motif
568 for protein interaction. Indeed, multiple reports from the literature suggest that the 3' end of
569 miRs are an essential element. For example, the 3' terminal 7 nucleotides of miR-382 were
570 observed to be necessary for its rapid decay (Bail *et al*., 2010). Furthermore, the terminal 3'
571 nucleotide has been shown to be monoadenylated by GLD2 causing a stabilizing phenotype in
572 a subset of miRs expressed in human fibroblasts (D'Ambrogio *et al*., 2012); however, GLD2-
573 catalyzed monoadenylation of miRs had no stabilizing effect in the hippocampus, providing
574 further evidence of tissue specific regulatory pathways (Mansur *et al*., 2016). In *Arabidopsis*
575 *thaliana*, a 3' to 5' exoribonuclease (Atrimmer) has been shown to be critical for miR turnover
576 (Wang *et al*., 2018), whereas the 3' to 5' exoribonuclease, DIS3L2, was observed to degrade
577 miRs in mammalian cell lines (Haas *et al*., 2016), further supporting the notion that the 3'
578 terminus can serve as a critical recognition element in miR processing and degradation.
579 Interestingly, our data showed that the 5' uracil of miR-9-5p was also important for conferring

stability, as removal of this nucleotide, representing an endogenous miR-9-5p isomiR, resulted in enhanced stability compared to the canonical sequence (Fig. 6D). This finding is interesting in the context of recent reports demonstrating that this miR-9-5p isomiR can be generated by alternative Drosha cleavage of primary miR-9 (Bofill-De Ros *et al*., 2018). This isomiR shifts the seed sequence of the miR, thereby expanding the scope of its respective mRNA targets. Functionally, it was identified that prevalence of this miR-9-5p isoform correlated with tumor progression in low-grade glioma (Bofill-De Ros *et al.,* 2018), suggesting that its inherent stability could contribute to unhinged, and even detrimental, downstream consequences in neural pathophysiology. Our degradation assays showed that little, if any, degradation of miR-9-5p and -3p occurred at the 5' end, based on total densitometry of all bands, including the smaller degradation products, between the initial to the final timepoint. However, Meziane and colleagues showed that the decapping enzyme DcpS was critical in determining the degradation kinetics of miRs by recruiting the 5' to 3' exoribonuclease XRN2 to the processing site in both *C. elegans* and in human model systems (2013, 2015), allowing for the possibility of XRN2 is a contributor of 5'-initiated miR-9-5p and -3p degradation. These *cis* contributions of even single nucleotides in altering degradation kinetics propose the exciting possibility that other neuronal miRs, which vary in their nucleotide compositions, may all exhibit unique degradation profiles in the central nervous system.

Overall, we have shown that miR-9-5p degradation kinetics are likely very rapid in the intact rat brain, consistent with previous studies. However, miR-9-3p (passenger) degradation had not been previously characterized, and our data indicate that the passenger strand is more stable than the guide in neuronal cells, suggesting that it could have a more prominent role in the regulation of neuronal physiology. Furthermore, we provide evidence that the differential degradation kinetics of miR-9-5p and miR-9-3p can be explained, in part, by both *cis* and *trans* elements, underscoring the complexity of miR degradation in the central nervous system.

References

Amar, L., Benoit, C., Beaumont, G., Vacher, C. M., Crepin, D., Taouis, M., & Baroin-Tourancheau, A. (2012). MicroRNA expression profiling of hypothalamic arcuate and paraventricular nuclei from single rats using Illumina sequencing technology. Journal of Neuroscience Methods, 209(1), 134–143.

Baccarini, A., Chauhan, H., Gardner, T. J., Jayaprakash, A. D., Sachidanandam, R., & Brown, B. D. (2011). Kinetic analysis reveals the fate of a MicroRNA following target regulation in mammalian cells. Current Biology, 21(5), 369–376.

Bail, S., Swerdel, M., Liu, H., Jiao, X., Goff, L. A., Hart R. P., & Kiledjian M. (2010). Differential regulation of microRNA stability. RNA, 16(5), 1032–1039.

Bitetti, A., Mallory, A. C., Golini, E., Carrieri, C., Carreño Gutiérrez, H., Perlas, E., Perez-Rico Y., Tocchini-Valentini G., Enright A., Norton W., Madillo S., O'Carroll D., & Shkumatava, A. (2018). MicroRNA degradation by a conserved target RNA regulates animal behavior. Nature Structural and Molecular Biology, 25(3), 244–251.

Bofill-De Ros, X., Kasprzak, W. K., Bhandari, Y., Fan, L., Cavanaugh, Q., Jiang, M., Dai L., Yang A., Shao T., Shapiro B., Wang Y., & Gu, S. (2019). Structural Differences between Pri-miRNA Paralogs Promote Alternative Drosha Cleavage and Expand Target Repertoires. Cell Reports, 26(2), 447–459.

Chatterjee, S., & Großhans, H. (2009). Active turnover modulates mature microRNA activity in Caenorhabditis elegans. Nature, 461(7263), 546–549.

Coolen, M., Katz, S., & Bally-Cuif, L. (2013). miR-9: a versatile regulator of neurogenesis. Frontiers in Cellular Neuroscience, 7.

D'Ambrogio, A., Gu, W., Udagawa, T., Mello, C. C., & Richter, J. D. (2012). Specific miRNA Stabilization by Gld2-Catalyzed Monoadenylation. Cell Reports, 2(6), 1537–1545.

De La Mata, M., Gaidatzis, D., Vitanescu, M., Stadler, M., Wentzel, C., Scheiffele, P., Filipowicz, W., & Großhans, H. (2015). Potent degradation of neuronal miRNAs induced by highly complementary targets. EMBO Reports, 16(4), 500–511.

Friedman, R. C., Farh, K. K. H., Burge, C. B., & Bartel, D. P. (2009). Most mammalian mRNAs are conserved targets of microRNAs. Genome Research, *19*(1), 92–105.

Fu, X., Shah, A., & Baraban, J. M. (2016). Rapid reversal of translational silencing: Emerging role of microRNA degradation pathways in neuronal plasticity. Neurobiology of Learning and Memory, 133, 225–232.

Gantier, M. P., McCoy, C. E., Rusinova, I., Saulep, D., Wang, D., Xu, D., Irving A., Behlke M., Hertzog P., Mackay F., & Williams, B. R. G. (2011). Analysis of microRNA turnover in mammalian cells following Dicer1 ablation. Nucleic Acids Research, 39(13), 5692–5703.

657 Ghini, F., Rubolino, C., Climent, M., Simeone, I., Marzi, M. J., & Nicassio, F. (2018).
658 Endogenous transcripts control miRNA levels and activity in mammalian cells by target-directed
659 miRNA degradation. Nature Communications, 9(1).
660
661 Giusti, S. A., Vogl, A. M., Brockmann, M. M., Vercelli, C. A., Rein, M. L., Trümbach, D., Wurst
662 W., Cazaila D., Stein V., Deussing J., & Refojo, D. (2014). MicroRNA-9 controls dendritic
663 development by targeting REST. eLife, 3.
664
665 Haas, G., Cetin, S., Messmer, M., Chane-Woon-Ming, B., Terenzi, O., Chicher, J., Kuhn L.,
666 Hammann P., & Pfeffer, S. (2016). Identification of factors involved in target RNA-directed
667 microRNA degradation. Nucleic Acids Research, 44(6), 2873–2887.
668
669 Kato, M. (2018). Target RNA-directed microRNA degradation; which controls which? Non-
670 Coding RNA Investigation, 2, 62–62.
671
672 Krol, J., Busskamp, V., Markiewicz, I., Stadler, M. B., Ribi, S., Richter, J Duebel J, Bicker
673 S, Fehling H.J., Schübeler D., Oertner T.G., Schratt G., Bibel M., Roska B., & Filipowicz, W.
674 (2010). Characterizing Light-Regulated Retinal MicroRNAs Reveals Rapid Turnover as a
675 Common Property of Neuronal MicroRNAs. Cell, 141(4), 618–631.
676
677 Kuscu, C., Kumar, P., Kiran, M., Su, Z., Malik, A., & Dutta, A. (2018). tRNA fragments (tRFs)
678 guide Ago to regulate gene expression post-transcriptionally in a Dicer-independent manner.
679 RNA, 24(8), 1093–1105.
680
681 Li, Y., Li, Z., Zhou, S., Wen, J., Geng, B., Yang, J., & Cui, Q. (2013). Genome-wide analysis of
682 human MicroRNA stability. BioMed Research International, 2013, 36875.

683

684 Luna, R. E., Arthanari, H., Hiraishi, H., Akabayov, B., Tang, L., Cox, C., Asano, K. (2013). The
685 interaction between eukaryotic initiation factor 1A and eIF5 retains eif1 within scanning
686 preinitiation complexes. Biochemistry, *52*(52), 9510–9518.

687

688 Madelaine, R., Sloan, S. A., Huber, N., Notwell, J. H., Leung, L. C., Skariah, G. Halluin C.,
689 Pasca S., Bejerano G., Krasnow M., Barres B., & Mourrain, P. (2017). MicroRNA-9 Couples
690 Brain Neurogenesis and Angiogenesis. Cell Reports, 20(7), 1533–1542.

691

692 Mansur, F., Ivshina, M., Gu, W., Schaevitz, L., Stackpole, E., Gujja, S., Edwards Y., & Richter,
693 J. D. (2016). Gld2-catalyzed 3′ monoadenylation of miRNAs in the hippocampus has no
694 detectable effect on their stability or on animal behavior. RNA, 22(10), 1492–1499.

695

696 Marzi, M. J., Ghini, F., Cerruti, B., De Pretis, S., Bonetti, P., Giacomelli, C., Gorski M., Kress T.,
697 Pelizzola M., Muller H., Amati B., & Nicassio, F. (2016). Degradation dynamics of microRNAs
698 revealed by a novel pulse-chase approach. Genome Research, 26(4), 554–565.

699

700 Meziane, O., Bossé, G. D., & Simard, M. J. (2013). The decapping scavenger enzyme DCS-1: A
701 new modulator of miRNA turnover. Cell Cycle, 12(17), 2715–2716.

702

703 Meziane, O., Piquet, S., Bossé, G. D., Gagné, D., Paquet, E., Robert, C., Tones M., & Simard,
704 M. J. (2015). The human decapping scavenger enzyme DcpS modulates microRNA turnover.
705 Scientific Reports, 5.

706

707 Park, J. H., Shin, S. Y., & Shin, C. (2017). Non-canonical targets destabilize microRNAs in
708 human Argonautes. Nucleic Acids Research, 45(4), 1569–1583.

Rädle, B., Rutkoswki, A., Ruzsics, Z., Friedel, C. C., Koszinowski, U. H., & Dölken, L. (2013). Metabolic labeling of newly transcribed RNA for high resolution gene expression profiling of RNA synthesis, processing and decay in cell culture. Journal of Visualized Experiments, (78).

Rao, Y. S., Mott, N. N., Wang, Y., Chung, W. C. J., & Pak, T. R. (2013). MicroRNAs in the aging female brain: A putative mechanism for age-specific estrogen effects. Endocrinology, 154(8), 2795–2806.

Rao, Y. S., Shults, C. L., Pinceti, E., & Pak, T. R. (2015). Prolonged ovarian hormone deprivation alters the effects of 17β-estradiol on microRNA expression in the aged female rat hypothalamus. Oncotarget, 6(35).

Richner, M., Victor, M. B., Liu, Y., Abernathy, D., & Yoo, A. S. (2015). MicroRNA-based conversion of human fibroblasts into striatal medium spiny neurons. Nature Protocols, 10(10), 1543–1555.

Rüegger, S., & Großhans, H. (2012). MicroRNA turnover: When, how, and why. Trends in Biochemical Sciences, 37(10), 436–446.

Sethi, P., & Lukiw, W. J. (2009). Micro-RNA abundance and stability in human brain: Specific alterations in Alzheimer's disease temporal lobe neocortex. Neuroscience Letters, 459(2), 100–104.

Sim, S. E., Bakes, J., & Kaang, B. K. (2014). Neuronal activity-dependent regulation of MicroRNAs. Molecules and cells, *37*(7), 511–517.

735

736 Sim, S. E. *et al.,* (2016). The Brain-Enriched MicroRNA miR-9-3p Regulates Synaptic Plasticity
737 and Memory. The Journal of Neuroscience, 36(33), 8641–8652.
738

739 Sun, A. X., Crabtree, G. R., & Yoo, A. S. (2013). MicroRNAs: Regulators of neuronal fate.
740 Current Opinion in Cell Biology, 25(2), 215–221,
741

742 Wang, X., Wang, Y., Dou, Y., Chen, L., Wang, J., Jiang, N. Guo C., Yao Q., Wang C., Liu L., Yu
743 B., Zheng B., Chekanova J., Ma J., & Ren, G. (2018). Degradation of unmethylated
744 miRNA/miRNA*s by a DEDDy-type 3′ to 5′ exoribonuclease Atrimmer 2 in Arabidopsis.
745 Proceedings of the National Academy of Sciences, 115(28), E6659–E6667.
746

747 Wang, Y., Sheng, G., Juranek, S., Tuschl, T., & Patel, D. J. (2008). Structure of the guide-
748 strand-containing argonaute silencing complex. Nature, 456(7219), 209–213.
749

750 Wightman, F. F., Giono, L. E., Fededa, J. P., & De La Mata, M. (2018). Target RNAs strike back
751 on MicroRNAs. Frontiers in Genetics, 2(9), 435.
752

753 Winter, J., & Diederichs, S. (2011). Argonaute proteins regulate microRNA stability. RNA
754 Biology, 8(6).
755

756 Yi, T., Arthanari, H., Akabayov, B., Song, H., Papadopoulos, E., Qi, H. H., Wagner, G. (2015).
757 EIF1A augments Ago2-mediated Dicer-independent miRNA biogenesis and RNA interference.
758 Nature Communications, 6.
759

760 Yuva-Aydemir, Y., Simkin, A., Gascon, E., & Gao, F.-B. (2011). MicroRNA-9. RNA Biology, 8(4),
761 557–564.
762
763 Zhang, Z., Qin, Y. W., Brewer, G., & Jing, Q. (2012). MicroRNA degradation and turnover:
764 Regulating the regulators. Wiley Interdisciplinary Reviews: RNA, 3(4), 593–600.
765
766
767 **Figure Legends**
768
769 **Figure 1. miR-9-3p was more stable than miR-9-5p in a hypothalamic cell line. A)** Gel
770 electrophoresis of ^{32P}-labeled miR-9-5p and miR-9-3p showing bands at their correct size: 23
771 and 22 nucleotides (nT), respectively. **B)** Representative gel image of miR-9-5p and miR-9-3p
772 degradation over time (min.) following incubation in hypothalamic-derived neuronal cell (IVB)
773 lysate for 0, 15, 60, 120, or 240 min. **C)** Scatterplot of normalized densitometry values analyzed
774 from gel images and fit with an exponential decay function (black line = miR-9-5p; red line =
775 miR-9-3p; N = 4/group). **D)** Normalized densitometry values at the 60 min. time point for miR-9-
776 5p and miR-9-3p. Data are represented as mean ± SEM (N = 4/group). **E)** Mean half-lives of
777 miR-9-5p and miR-9-3p derived from best-fit exponential decay functions. Results are
778 represented as mean ± SEM (N = 4/group), and horizontal line overlaying the bar graph
779 indicates the median. Data were analyzed using a two-sample t-test.
780
781 **Figure 1-1. AGO2 binds to ^{32P}-labeled miR-9-5p and miR-9-3p.** Representative gel image of
782 ^{32P}-labeled miR-9-5p, miR-9-3p, and an equimolar equivalent mixture of both following
783 immunoprecipitation with **A)** AGO2, **B)** IgG control, and **C)** AGO4 and β-actin.
784

Figure 2. miR-9-3p was more stable than miR-9-5p following transcriptional inhibition. Hypothalamic-derived IVB cells were treated with the transcriptional inhibitor actinomycin D for 2 hours. Cells were lysed at 0, 15, and 60 minutes following treatment, total RNA was isolated, and RT-qPCR was performed for miR-9-5p and miR-9-3p (N = 5/group). Results were analyzed using the ΔΔCt method and are represented as mean fold change ± SEM, and horizontal line overlaying the bar graph indicates the median. Data were analyzed by two-way ANOVA with time and miR construct as factors. A Tukey's post hoc test was performed to determine statistically significant differences between group means.

Figure 3. miR-9-3p was more stable than miR-9-5p in a brain region dependent manner. **A)** Representative gel image of ^{32P}-labeled miR-9-5p and miR-9-3p following incubation with rat brain lysate (N = 3/brain region). POA-preoptic area, vHIPP-ventral hippocampus, SON-supraoptic nucleus **B)** Scatterplot of normalized densitometry values analyzed from gel images and fit with an exponential decay function showing brain region specific degradation kinetics of miR-9-5p and miR-9-3p. **C)** Mean half-lives of miR-9-5p and miR-9-3p in various brain regions derived from best-fit exponential decay functions. Results are represented as mean ± SEM (N = 3/group), and horizontal line overlaying the bar graph indicates the median. Data were analyzed by two-way ANOVA with brain region and miR construct as factors. A Tukey's post hoc test was performed to determine statistically significant differences between group means.

Figure 4. Rapid miR-9-5p degradation in rat brain (SON) tissue lysate was dependent on protein concentration of the lysate. A) Representative gel image of ^{32P}-labeled miR-9-5p following incubation with 1:10, 1:100, and 1:1000 dilutions of rat brain (SON) lysate, lysis buffer alone, or following SON lysate treatment with proteinase K for 60 min. at 60°C. **B)** Scatterplot of

809 normalized densitometry values analyzed from gel images and fit with an exponential decay
810 function showing concentration dependent degradation kinetics of miR-9-5p (N = 4/group).
811
812 **Figure 5. Degradation of miR-9-5p was slower in primary astrocytes compared to rat**
813 **brain (SON) tissue lysate. A)** Representative gel image of ^{32P}-labeled miR-9-5p following
814 incubation with rat brain tissue (SON) lysate or rat primary astrocytes for 0, 1, 15, 60, or 120 min
815 (N = 3). **B)** Scatterplot of normalized densitometry values analyzed from gel images and fit with
816 an exponential decay function. **C)** Mean half-lives of miR-9-5p were derived from best-fit
817 exponential decay functions. Results are represented as mean ± SEM (N = 3/group), and
818 horizontal line overlaying the bar graph indicates the median. Data were analyzed using a two-
819 sample T-test.
820
821 **Figure 6. Nucleotide sequences at both the 5' and 3' end contribute to miR-9 stability. A)**
822 Schematic diagram showing the nucleotide compositions of the miR-9 constructs: 5P = full-
823 length canonical miR-9-5p, 3P = full-length canonical miR-9-3p, 5P* = miR-9-5p with a UGA to
824 AGU substitution at the 3' end, 3P* = miR-9-3p with an AGU to UGA substitution at the 3' end,
825 5p isomiR = miR-9-5p with a U deletion at the 5' end. Red font indicates nucleotide variation
826 from canonical sequences. **B)** Representative gel image showing the degradation kinetics of ^{32P}-
827 labeled miR-9-5p, -3p, 5p*, 3p*, and 5p isomiR following incubation in rat brain (SON) lysate for
828 0, 1, 15, 60, or 120 min. **C)** Scatterplot of normalized densitometry values analyzed from gel
829 images and fit with an exponential decay function showing that both 5' and 3' end modifications
830 affect stability (N = 3-4/group). **D)** Normalized densitometry values at the 1 min. time point for
831 the miR-9-5p, 5p*, and isomiR constructs. Results are represented as mean ± SEM (N = 3-
832 4/group). Data were analyzed by one-way ANOVA with miR construct as the categorical factor.
833 A Tukey's post hoc test was performed to determine statistically significant differences between
834 group means. **E)** Normalized densitometry values at the 15 min. time point for miR-9-3p and -

3p*. Results are represented as mean ± SEM (N = 3-4/group), and horizontal line overlaying the bar graph indicates the median. Data were analyzed using a two-sample t-test.

Figure 7. miR-9-5p and miR-9-3p were associated with distinct proteins in the rat ventral hippocampus. A) Various length nucleotides matching the sequence for miR-9-5p (23, 16, 12 nT) and miR-9-3p (22, 16, 12 nT) were modified with a biotin tag on the 5' end and incubated with lysate from the rat ventral hippocampus (vHIPP). **B)** Biotinylated miR constructs were purified using streptavidin-coated magnetic beads and resolved on a 10% SDS PAGE gel followed by Coomassie G-250 staining. Red box indicates gel bands that were dissected for in-gel digestion followed by mass spectrometry. **C)** Venn diagrams with number of unique proteins identified by mass spectrometry compared between miR-9-5p and miR-9-3p at various sequence lengths plus beads only, or **D)** comparison of identified proteins within miR-9-5p (23, 16, 12 nT) and miR-9-3p (22, 16, 12 nT). Red color numbers indicate proteins unique to each construct and black numbers indicate proteins common between constructs. Blue lettering indicates known RNA binding proteins.

Table 1. Statistical analysis

Table 2. List of unique proteins that were associated with various length nucleotides matching the sequence for miR-9-5p (23, 16, 12 nT) and miR-9-3p (22, 16, 12 nT), as identified by mass spectrometry using PEAKS™ software.

Table 3. Table summarizing proteins identified by mass spectrometry that were associated with various length nucleotides matching the sequence for miR-9-5p (23, 16, 12 nT) and miR-9-3p (22, 16, 12 nT) and organized by functional class according to Panther gene ontology analysis.

Fig. 1

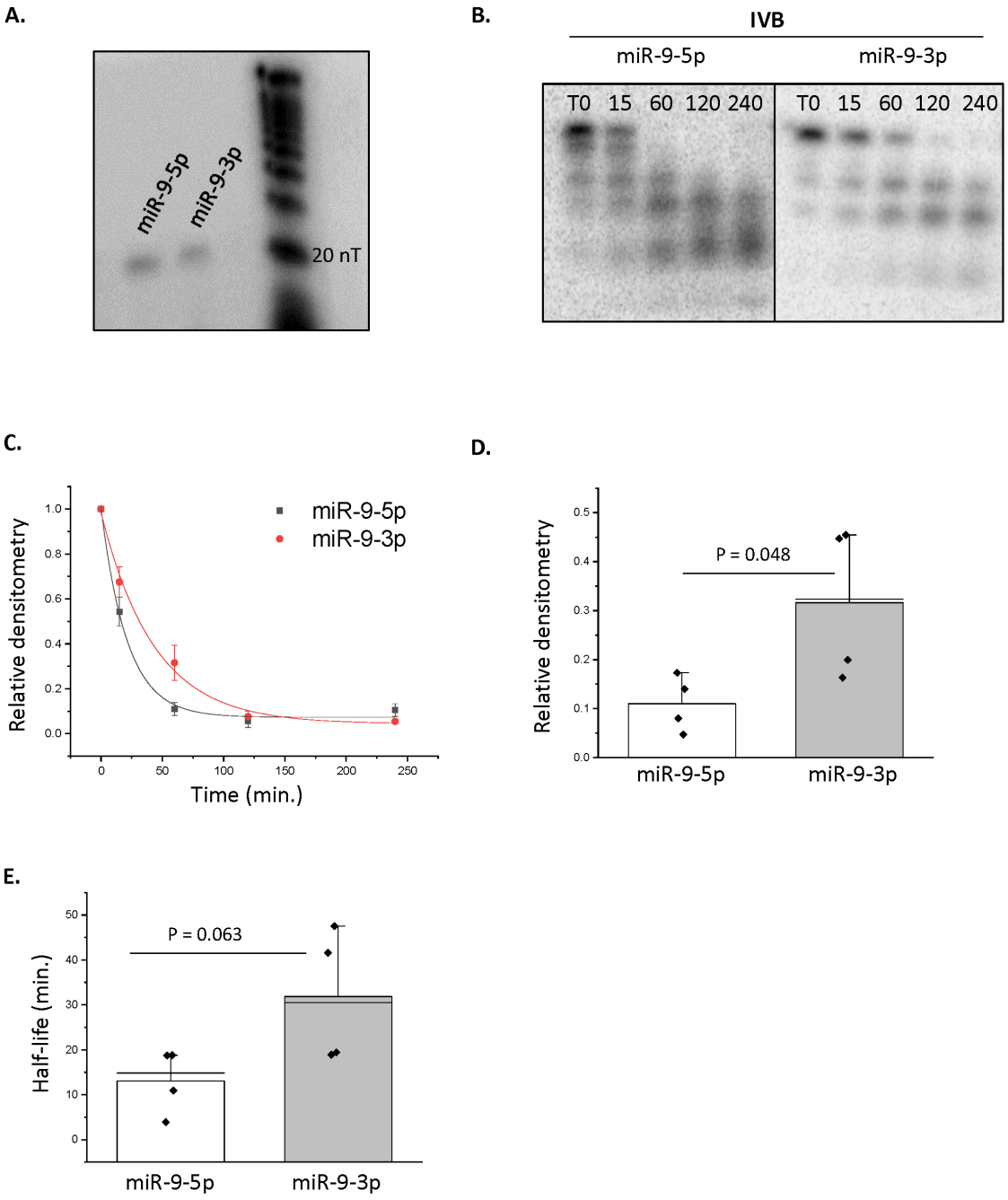

Fig. 2

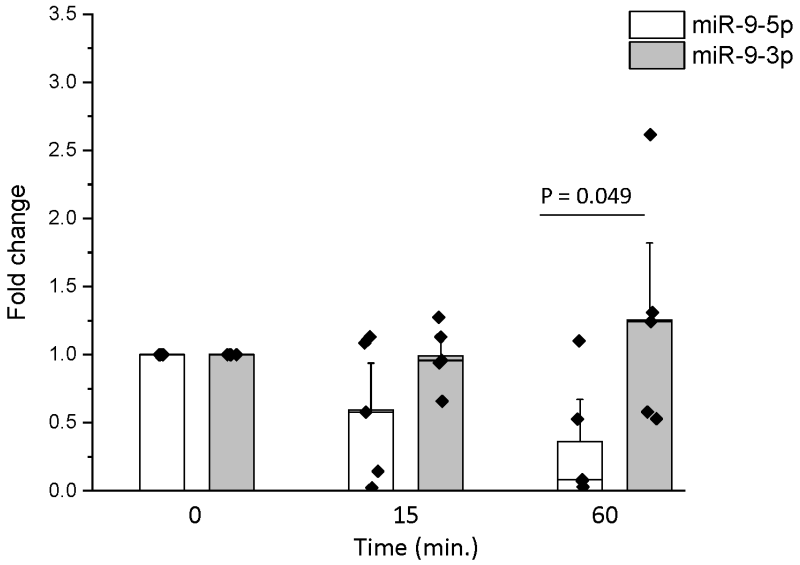

Fig. 3

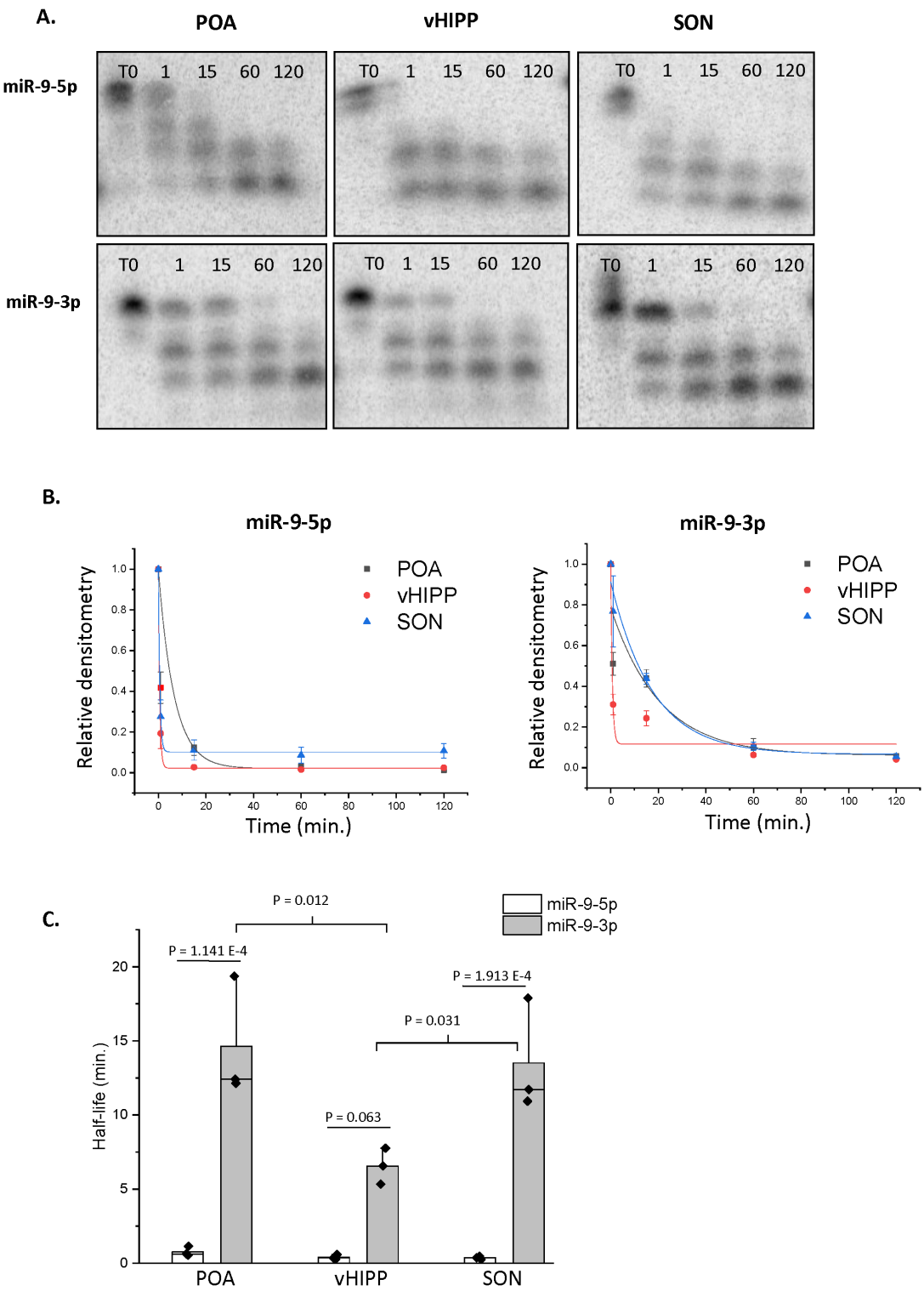

Fig. 4

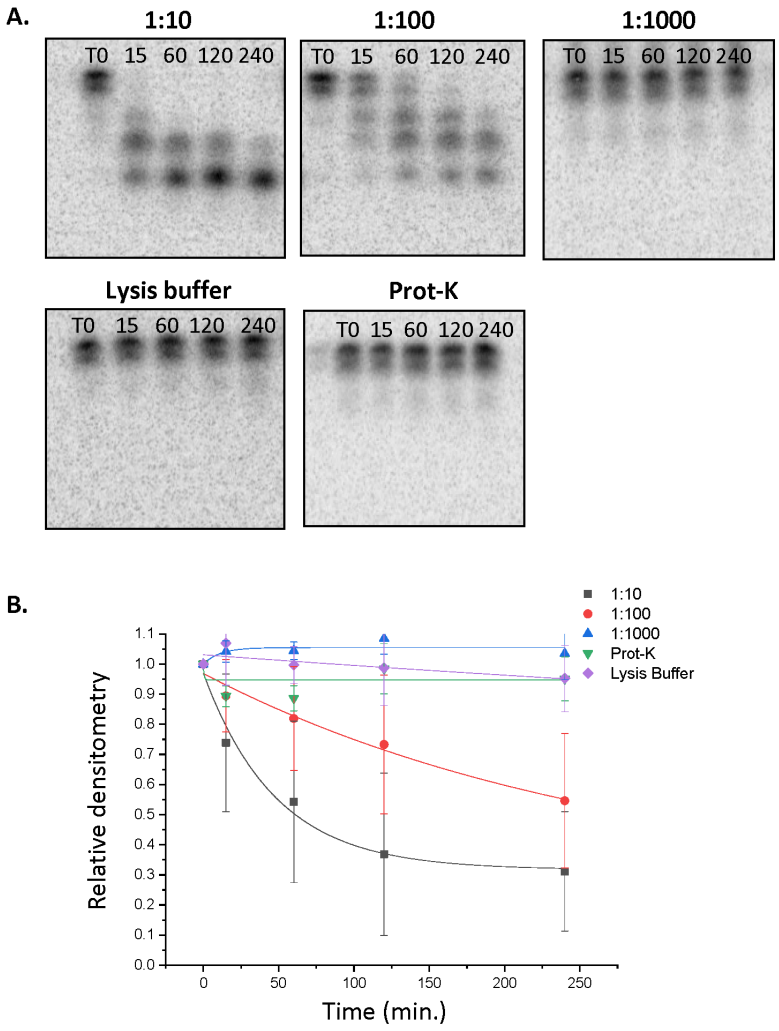

Fig. 5

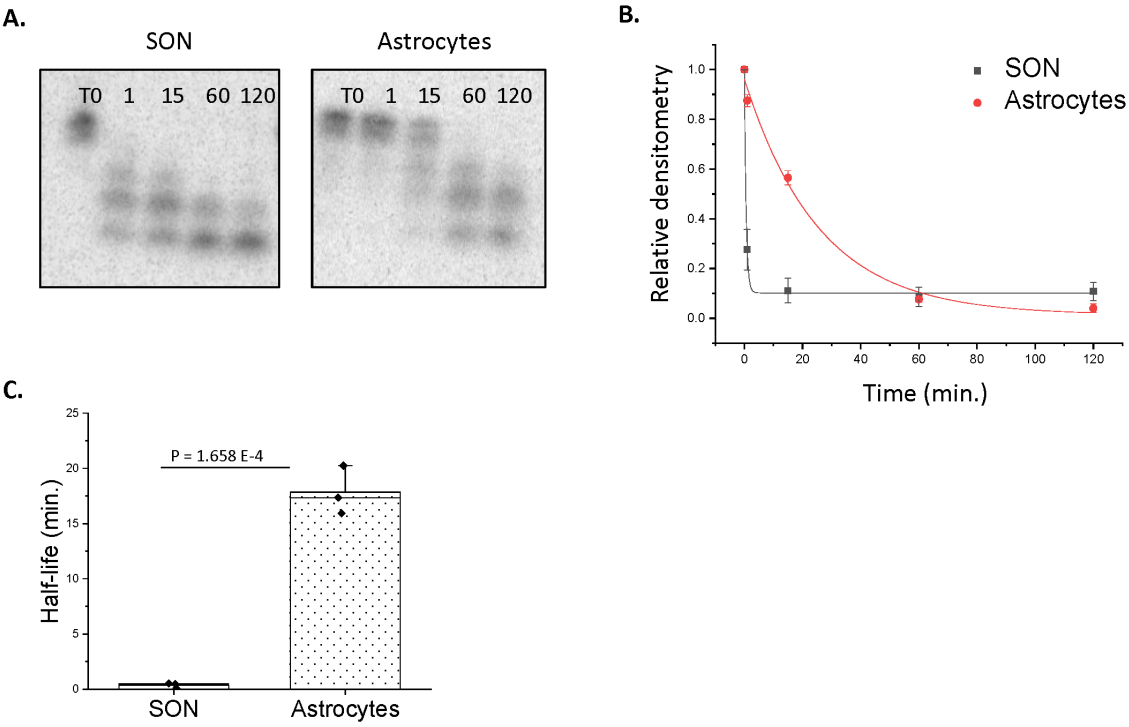

Fig. 6

A.

5P: UCUUUGGUUAUCUAGCUGUAUGA
3P: AUAAAGCUAGAUAACCGAAAGU
5P*: UCUUUGGUUAUCUAGCUGUAAGU
3P*: AUAAAGCUAGAUAACCGAAUGA
5p isomiR: _CUUUGGUUAUCUAGCUGUAUGA

B.

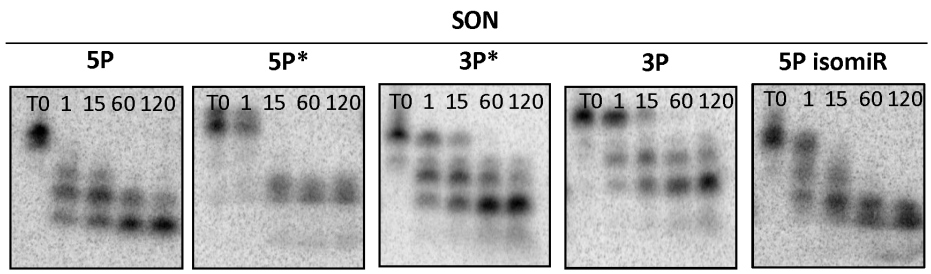

C.

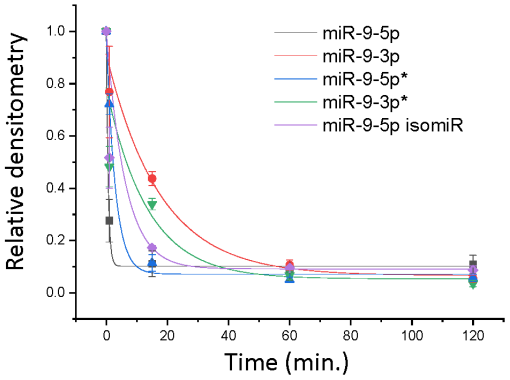

D.

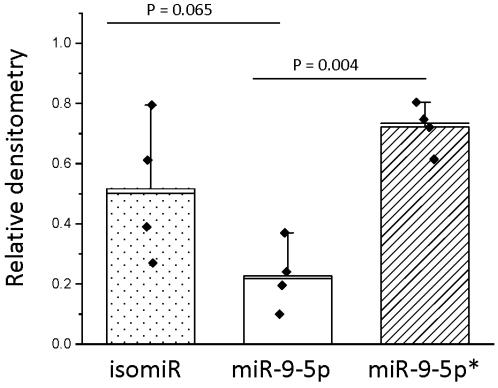

E.

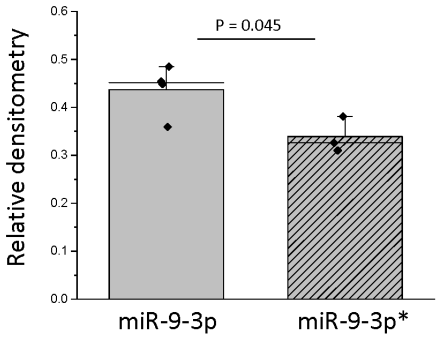

Fig. 7

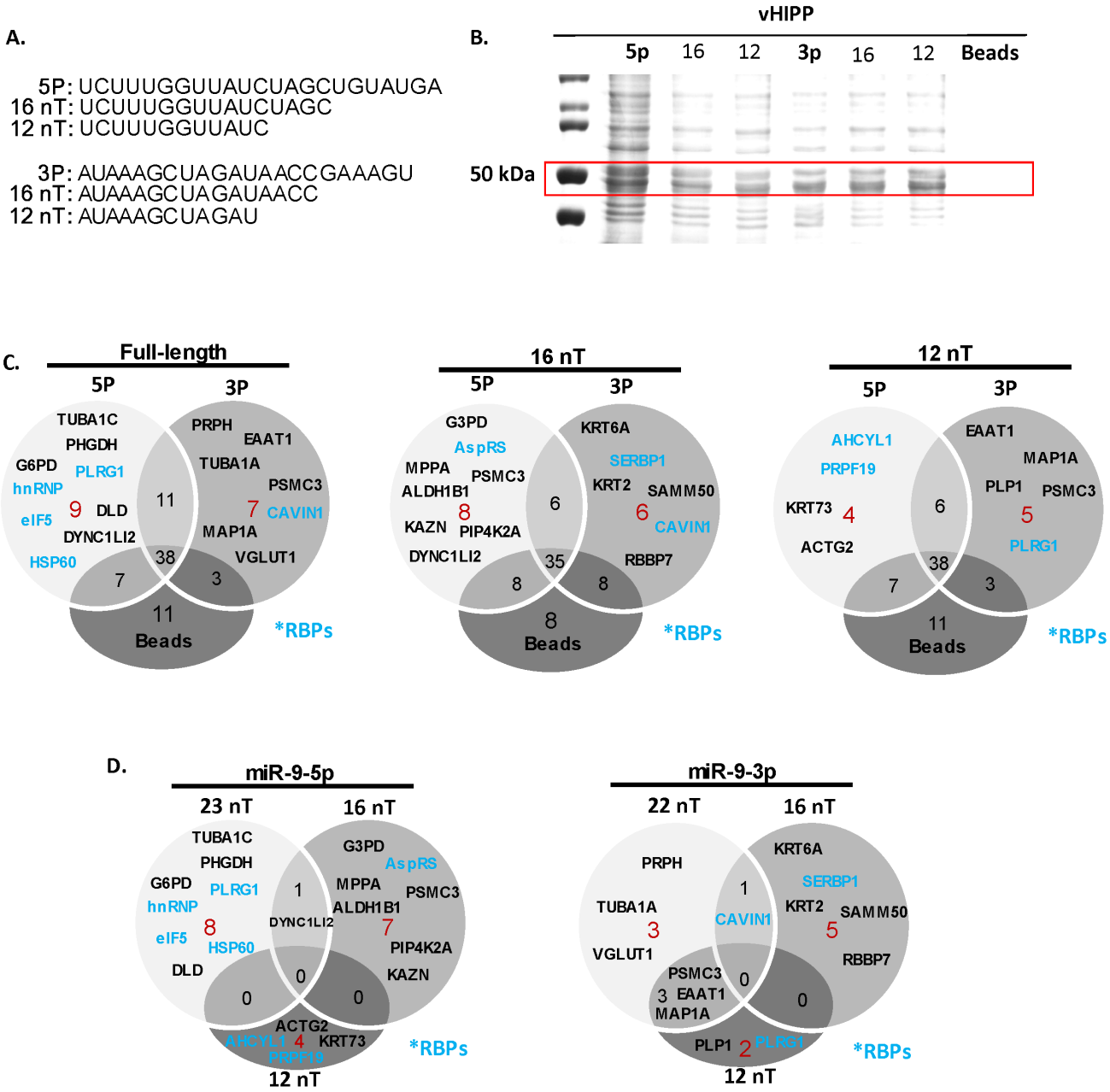

Table 1. Statistical Analysis

Dataset	Data structure	Type of test	Power
Figure 1D	Normal distribution	Two sample T-test	$p = 0.048$
Figure 1E	Normal distribution	Two sample T-test	$p = 0.063$
Figure 2	Normal distribution	Two-way ANOVA Tukey's HSD	Time: $F_{(1,24)} = 0.646$, $p = 0.533$ miR: $F_{(1,24)} = 6.724$, $p = 0.016$ Time x miR interaction: $F_{(1,24)} = 2.414$, $p = 0.111$
Figure 3C	Normal distribution	Two-way ANOVA Tukey's HSD	Brain region: $F_{(1,12)} = 5.543$, $p = 0.020$ miR: $F_{(1,12)} = 100.365$, $p = 3.511 \times 10^{-7}$ Brain region x miR interaction: $F_{(1,12)} = 4.979$, $p = 0.027$
Figure 5C	Normal distribution	Two sample T-test	$p = 1.658 \times 10^{-4}$
Figure 6D	Normal distribution	One-way ANOVA	$F_{(2,9)} = 10.119$, $p = 0.005$
Figure 6E	Normal distribution	Two sample T-test	$p = 0.045$

Table 2. List of unique proteins that were associated with various length nucleotides matching the sequence for miR-9-5p (23, 16, 12 nT) and miR-9-3p (22, 16, 12 nT), as identified by mass spectrometry using PEAKS™ software.

5P 23 nT

Protein
D-3-phosphoglycerate dehydrogenase
Glucose-6-phosphate 1-dehydrogenase
Heterogeneous nuclear ribonucleoprotein
60 kDa heat shock protein
Eukaryotic translation initiation factor 5
Cytoplasmic dynein 1 light intermediate chain 2
Tubulin alpha-1C chain
Dihydrolipoyl dehydrogenase
Pleiotropic regulator 1

5P 16 nT

Protein
Glyceraldehyde-3-phosphate dehydrogenase
Aspartate--tRNA ligase, cytoplasmic
Mitochondrial-processing peptidase subunit alpha
Kazrin
Cytoplasmic dynein 1 light intermediate chain 2
26S proteasome regulatory subunit 6A
Phosphatidylinositol 5-phosphate 4-kinase type-2 alpha
Aldehyde dehydrogenase X

5P 12 nT

Protein
S-adenosylhomocysteine hydrolase-like protein 1
Pre-mRNA-processing factor 19
Keratin, type II cytoskeletal 73
Actin, gamma-enteric smooth muscle

3P 22 nT

Protein
Peripherin
Excitatory amino acid transporter 1
Microtubule-associated protein 1A
Tubulin alpha-1A chain
Caveolae-associated protein 1
Vesicular glutamate transporter 1
26S proteasome regulatory subunit 6A

3P 16 nT

Protein
Caveolae-associated protein 1
Keratin, type II cytoskeletal 6A
Plasminogen activator inhibitor 1 RNA-binding protein
Sorting and assembly machinery component 50 homolog
Keratin, type II cytoskeletal 2 epidermal
Histone-binding protein RBBP7

3P 12 nT

Protein
Excitatory amino acid transporter 1
Pleiotropic regulator 1
Microtubule-associated protein 1A
26S proteasome regulatory subunit 6A
Myelin proteolipid protein

Table 3. Table summarizing proteins identified by mass spectrometry that were associated with various length nucleotides matching the sequence for miR-9-5p (23, 16, 12 nT) and miR-9-3p (22, 16, 12 nT) and organized by functional class according to Panther gene ontology analysis.

	Cytoskeletal	Membrane trafficking	Protein modifying	Transporter	Metabolism	Nucleic acid binding	Translation
miR-9-5p	22.2%	—	—	—	33.3%	11.1%	11.1%
16 nT	12.5%	—	25%	—	37.5%	—	12.5%
12 nT	40%	—	—	—	20%	—	—
miR-9-3p	28.6%	14.3%	14.3%	28.6%	—	—	—
16 nT	—	16.7%	—	—	—	16.7%	—
12 nT	20%	—	20%	20%	—	—	—